Thermally Activated Wetting Dynamics in the Presence of Surface Roughness
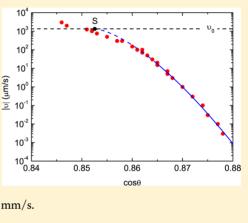
Kristina Davitt,*[,†] Michael S. Pettersen,[‡] and Etienne Rolley[†]

[†]Laboratoire de Physique Statistique, Ecole Normale Supérieure, UPMC Univ Paris 06, Université Paris Diderot, CNRS, 24 rue Lhomond, 75005 Paris, France

[‡]Department of Physics, Washington and Jefferson College, Washington, Pennsylvania 15301, United States

ABSTRACT: From simple models of thermally activated contact line dynamics far below the depinning transition, one expects the velocity to depend exponentially on the applied force and the activation area to be the size of the defects on the surface. We study contact line motion on evaporated gold films and find that the dynamics are activated, but the activation area is not straightforwardly linked to the surface roughness. Surprisingly, the activation area can be significantly smaller than any features on the surface. Furthermore, it depends strongly on the liquid. We show that this indicates that the line is close to the depinning threshold at experimentally accessible velocities. A model based on independent defects is developed and used to show deviations from the purely exponential law. The dynamics are written entirely in terms of properties of the surface and partially wetting liquid. In addition, we are able to show that the region of validity of models of thermal activation on mesoscopically rough surfaces typically corresponds to velocities of less than 1 mm/s.

INTRODUCTION

How a liquid spreads on a solid is strongly influenced by the disorder on the surface. This is at once a practical issue — as many ordinary surfaces are either chemically or topographically heterogeneous, if not on the optical scale then at the nanometric scale — and a general one[1] since it is an example of an elastic interface in a disordered medium, much like magnetic domain walls[2] or crack front propagation.[3]

In accordance with Young's law, $\gamma \cos \theta_{eq} = \gamma_{SV} - \gamma_{SL}$, the equilibrium contact angle θ_{eq} for a liquid on a solid surface is determined by the set of interfacial tensions between the liquid, vapor, and solid ($\gamma = \gamma_{LV}$, γ_{SV}, γ_{SL}). However, one finds that θ_{eq} is not experimentally accessible, but that the measured angle depends on the history of the contact line. Consider a drop placed on a solid surface: the contact angle slowly decreases as it relaxes toward equilibrium, and the velocity of the contact line gets progressively slower. In practice, equilibrium is never strictly achieved and the velocity never reaches zero, even if it is well below experimental resolution. Instead, it has become standard to report angles for very slowly advancing (θ_A) or receding (θ_R) contact lines, which allows us to define a hysteresis $H = \gamma(\cos \theta_R - \cos \theta_A) > 0$. It has been understood for some time that this hysteresis is attributed to pinning of the contact line on disorder present on the solid surface.[4,5] On the other hand, the dynamics of this pinning and depinning process, or how the velocity of the contact line depends on the unbalanced Young force at low velocity, is still very often neglected.

There are a number of well-developed models of wetting dynamics, including the molecular kinetic theory (MKT), which considers dissipation at the contact line due to molecular-scale activated processes,[6] and hydrodynamic models, which account for bulk viscous dissipation[5] that becomes important for larger capillary numbers, $Ca = \eta v/\gamma$, where η is the liquid viscosity and v the velocity. It is important to note that much like the Young equation, these models were developed with the assumption of perfect surfaces and one can ask under what conditions they can be used in the presence of disorder. In this article, we study contact line motion at very low capillary numbers, $Ca = 10^{-5}$ to 5×10^{-11}, on surfaces with mesoscale roughness (10−100 nm) and therefore expect *a priori* to find that activated processes dominate.

The relationship between nanoroughness and hysteresis[7,8] has been studied experimentally, and the hysteresis has been found to depend on the size and density of defects. Also, measurements of the dynamics on molecular layers[9,10] have been made; however, to our knowledge no systematic study of activated dynamics has been done on surfaces of controlled topographical disorder in order to directly link measurable surface and liquid properties to the dynamics. In a previous study of liquid hydrogen on evaporated cesium surfaces,[11] it was found that the activation area was on the order of the size of the grains of cesium, but it is difficult to modify and measure the disorder in cryogenic systems and a limited range of velocities was explored. Here, we have developed a room-temperature analog to this system where (i) the surface

roughness can easily be altered and imaged, (ii) the contact angle and γ can be modified independently in order to examine their individual effect, and (iii) steady-state motion of the contact line down to velocities of 1 nm/s can be achieved.

First, we recall the oft-used MKT-form of the contact line dynamics. At zero temperature, there is a well-defined pinning force that must be overcome in order to move the contact line. At a temperature T, thermal activation rounds this transition and for a given energy barrier, E_b, one expects the contact line to move at very low velocity described by an Arrhenius-type escape rate:

$$\tau^{-1} = \nu \, \exp\left(\frac{-E_b}{k_B T}\right) \tag{1}$$

The energy barrier can be explicitly written in terms of the activation free energy of wetting, E_a, and the applied force which acts to reduce the barrier, whereupon the velocity of the contact line can be written

$$v = v_0 \, \exp\left(\frac{-1}{k_B T}\left(E_a - \frac{\sigma f}{2}\right)\right) \tag{2}$$

This is formally equivalent to the original MKT,[12] in which case v_0 is usually written as the thermal attempt frequency $\nu = k_B T / h$ multiplied by a molecular-scale jump size, where h is Planck's constant, and σ^{-1} is the number of adsorption sites per unit area. The force per unit length on the contact line is the unbalanced Young force, $f = \pm \, \gamma(\cos \theta_{eq} - \cos \theta)$, where the $\pm$ refers to advancing/receding and θ is the dynamic contact angle.

This picture assumes that the energy barrier is linearly reduced by the applied force, which is reasonable for very small forces where $E_b \approx E_a$. In the case of activated contact line dynamics on a rough surface, how to write v_0 and E_a and how to identify σ are open questions. One may even question the validity of the form of eq 2 because it is possible to attain a regime where $E_b \ll E_a$. These questions will be addressed in this paper, but we note that in practice, even in the case of large forces, the functional form of eq 2 can be used as a linearization over some small range of velocity. We first turn our attention to σ and note that it can be determined from experimentally measured dynamics and eq 2 without any assumptions on the expression of v_0 or E_a. Generally, σ is thought of as the surface that the contact line sweeps over as it jumps from one equilibrium position to another. In this picture, it is the disorder on the surface that creates the energy landscape over which the contact line moves, and thus σ is related to the scale of the disorder. If one were to naïvely apply MKT to this mesoscale problem, one would identify the activation area as simply the lateral scale of the disorder. We will see that the relationship is not so straightforward. One can also ask how σ is affected, if at all, by the contact angle and the liquid−vapor surface tension, γ. We find that there is a strong dependence of σ on the liquid. To explain these observations, we develop an alternative model to eq 2, valid for the dynamics at large applied forces. For this, we consider the activated escape from a metastable well subject to a steadily increasing bias, a problem that has recently received attention in the field of atomic friction.[13,14] This enables us to relate the dynamics directly to measurable properties of the disordered solid surface and the liquid.

■ MATERIALS AND METHODS

Materials. Silicon wafers were purchased from Siltronix SAS ([100], roughness <7 Å) and cleaned with a solvent rinse, followed by a piranha etch and oxygen plasma cleaning immediately prior to the metalizations. Gold was purchased from Neyco S.A. (purity >99.99%) and thermally deposited under vacuum at an average rate of 0.22 nm/s. The substrate temperature was held constant at either 25 or 200 °C. For the former, a 3 nm layer of chromium was evaporated prior to the gold in order to improve adhesion, but for the latter, it was omitted as chromium diffuses in gold at high temperature. Alkanethiols ($HS(CH_2)_n X$) were purchased from Sigma-Aldrich and used as-received: hexanethiol ($n = 5$, X = CH_3, 95%), dodecanethiol ($n = 11$, X = CH_3, ≥98%), octadecanethiol ($n = 17$, X = CH_3, 98%), methyl 3-mercaptopropionate ($n = 2$, X = $COOCH_3$, 98%), and 1H,1H,2H,2H-perfluoro-1-decanethiol ($n = 2$, X = $(CF_2)_7CF_3$, >96%). To produce self-assembled monolayers (SAMs), alkanethiols were diluted in ethanol (Sigma-Aldrich, absolute) to 1 mM and used immediately on gold films after evaporation. Wetting studies were performed after anywhere from 12 h to 8 days of immersion in the thiol solution without noticeable degradation, and each sample was used only once. Wetting liquids were deionized ultrapure water (18 MΩ cm), decane (≥99%), tetradecane (≥99%), and dimethyl sulfoxide (DMSO anhydrous, ≥99.9%).

Rough Surfaces. In this study, the disorder is due to the nanoscale topography that is naturally obtained when growing thin metallic films by thermal evaporation. The resulting morphology depends on the substrate, the evaporation rate, the final film thickness, and the temperature of the substrate during evaporation.[15,16] We use silicon substrates and evaporate gold films with thicknesses between 10 and 100 nm, with the substrate held at either 25 or 200 °C. The gold films are imaged under AFM (Bruker Nanoscope III, tapping mode) in order to quantify the roughness. Bare gold films are high-energy surfaces that are completely wetted by most liquids, therefore, we use self-assembled monolayers of alkanethiols to render the surface nonwetting. The contact angle can be changed by using a different termination group. It is assumed that the SAM does not significantly alter the disorder from the point of view of wetting dynamics for reasons that are outlined below.

Contact Angle Measurements. Prepared substrates are dipped vertically into a liquid bath at a velocity controlled by a motorized stage. The hysteresis is evaluated with the contact line advancing and receding at a reference velocity (here, taken systematically as 10 μm/s). To measure the dynamics, the velocity is programmed to make controlled jumps around this reference velocity, and the resulting change in the capillary rise, Δh, is measured under the microscope. Figure 1 shows an example of a jump in the capillary rise due to such a jump in velocity. The inset illustrates the principle of measurement. The dynamic contact angle is then deduced from the capillary rise $h = L_c[2(1 - \sin \theta)]^{1/2}$, where $L_c = [\gamma/(\rho g)]^{1/2}$ is the capillary length and ρ is the liquid density.

This method provides a very accurate measurement of the *variations* in the contact angle and is therefore well-adapted to studies of contact line dynamics. However, the bulk liquid level is difficult to measure optically and therefore the advancing (receding) angle at the reference velocity is determined in a separate experiment where the liquid is ejected from (taken up by) a syringe to form a moving drop on the substrate. (Insets in
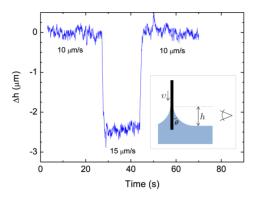
Figure 1. Change in the capillary rise due to a change of velocity of an advancing contact line between the reference of 10 μm/s and a velocity of 15 μm/s. For this particular sample (liquid decane with θ_A = 30°), the resulting variation in the contact angle is 0.09°. The inset shows the sample, viewed from the side, being dipped into a liquid bath, which creates an advancing contact line. A microscope facing the sample surface images the contact line, from which the capillary rise is found.

Figure 5a show typical images.) For example, Δh is measured with an accuracy taken as ±0.25 μm, which yields an uncertainty on the variation in θ on the order of 0.01°. This is in contrast to the uncertainty in the absolute value of θ of a few degrees arising from imaging a drop.

In comparison to experiments where transient motions of the contact line are analyzed,[10] another advantage of this method is that the range of velocities explored can be very large. We use a motorized stage to obtain velocities from several millimeters per second down to 100 nm/s and a piezo-driven stage to reach 1 nm/s, an unprecedentedly low velocity for studies of contact line dynamics.

In practice, measurements are repeated by advancing and receding over the same sample area multiple times. On a typical substrate, the contact angle drifts by less than 1° from one advancing cycle to the next. Occasionally, a substrate appears to age from one cycle to the next, always becoming more wettable. Even in this case, the absolute contact angle drifts by only a few degrees over half a dozen cycles, and we do not observe any drift in the variations of the angle.

■ RESULTS

Activation Area and Roughness. Typical AFM images for 80 nm thick gold films evaporated at two different temperatures are shown in Figure 2. The 25 °C film exhibits grain sizes of roughly 20 nm and canyons between grains. Owing to the radius of curvature of the AFM tip (10 nm), one must be careful when extracting any details besides the grain center-to-center distance. The 200 °C film exhibits grains nearly an order of magnitude larger and canyons roughly 50 nm wide. An oft-cited measure of the topography is the root-mean-square roughness, R_{rms}; here it is 0.7 and 7.4 nm, respectively. To a first approximation in the simple model of wetting dynamics of eq 2, one expects to find σ to be related to the lateral size of the grains. As a measure of this scale, we have used the width of the autocorrelation of the height function[17] performed along the scan direction of each AFM image. By varying the film thickness and the substrate temperature, we obtain L_{corr} between 8 and 80 nm.

Figure 3 shows typical results for the dynamics measured on these surfaces. An activated regime appears at the lowest velocities and a fit to eq 2 yields σ. In the following, we use the expression activation length to mean $\sqrt{\sigma}$. We systematically use only data at velocities ≤20 μm/s and the advancing and receding branches are fit independently to yield potentially different $\sqrt{\sigma_A}$ and $\sqrt{\sigma_R}$.

Figure 4 shows the results from a series of experiments where the evaporation conditions have been varied, but the SAM and partially wetting liquid are the same. For the 25 °C gold films, we find both correlation lengths and activation lengths on the order of 10−20 nm. This is the same as obtained in previous wetting studies on cesium.[11] We note that the morphology of these films appear very similar to that of cesium,[17] which is not surprising given that the evaporations take place at similar fractions of the respective melting temperatures.[16]

Figure 4 also appears to show that the activation length depends very little on the topography. For advancing contact lines, the dependence is measurable; increasing L_{corr} by an order of magnitude yields activation lengths of 25 nm, or roughly 2
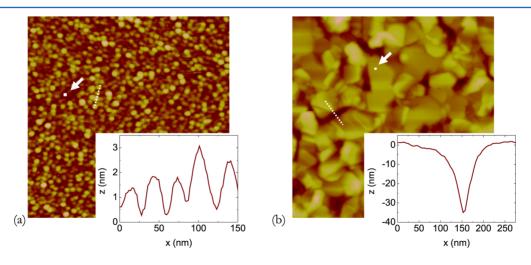

Figure 2. Typical tapping-mode AFM images of 80 nm gold films evaporated at 25 and 200 °C. In (a) the scan size is 1 × 1 μm, R_{rms} = 0.7 nm, and L_{corr} = 13.7 nm, whereas in (b) the scan size is 2 × 2 μm, R_{rms} = 7.4 nm, and L_{corr} = 70 nm. The white square superimposed on each image indicates the size of the activation area determined from the dynamics of tetradecane on a dodecanethiol SAM, $\sqrt{\sigma_A}$ = 16 nm and $\sqrt{\sigma_A}$ = 23 nm, respectively, and the inset shows the topography of the canyons between gold grains.
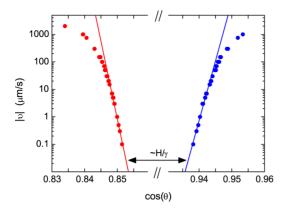
Figure 3. Wetting dynamics of liquid decane advancing (red) and receding (blue) on a gold surface evaporated at 25 °C and coated with a dodecanethiol SAM. The straight line shows the fit of the low velocity data to eq 2, from which the activation area σ is determined. Note the cut in the horizontal scale.
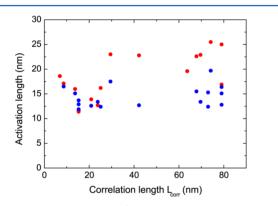

Figure 4. Activation lengths ($\sqrt{\sigma}$) deduced from the low velocity dynamics of advancing (red) and receding (blue) contact lines. Here, the surfaces are evaporated gold covered with a dodecanethiol SAM, and the liquid is tetradecane.

times larger. This is the first surprising result: despite very considerable changes in the surface morphology, the activation length changes very little. It calls into question the appealingly simple picture of the contact line being pinned between grains and making activated jumps where it sweeps over one grain at at time.

Superimposed on the AFM images in Figure 2 is a white square, indicating the activation area deduced from the respective dynamics. From the image of the large gold grains in particular, we find a second surprising observation: it appears that σ can be mesoscopic but still significantly smaller than any features on the surface.

Activation Area and Liquids. First, the dynamics of a series of partially wetting liquids, whose properties are shown in Table 1, were measured on surfaces of gold evaporated at 25 °C

Table 1. Properties of Partially Wetting Liquids at 23°C[a]

liquid	γ (mN/m)	η (mPa s)	ρ (kg/m³)	L_c (mm)	$\ln(v_0)$ (μm/s)
decane	23.55	0.86	728.8	1.81	7.2
tetradecane	26.3	2.21	761.3	1.88	6.2
DMSO	43.2	2.07	1097.4	2.00	6.3
water	72.3	0.96	997.54	2.72	7

[a]The spinodal velocity, v_0, is defined in eq 16c.

with a dodecanethiol SAM. Figure 5a summarizes the resulting activation lengths. This yields a third unexpected result: there is a strong dependence on γ, with larger surface tensions yielding systematically lower activation lengths, down to approximately 5 nm for water. Then, in order to investigate the effects of γ and θ independently, the termination group of the SAM was changed and measurements were made with the same liquids. Table 2 gives the average advancing and receding contact angles for each liquid and SAM combination used.

Statistical error bars are shown for a combination of surface and liquid that was repeated in 12 separate experiments. In any individual experiment, the fits are good, and the activation length can be extracted with some precision; however, identically prepared surfaces give some variation. For example, $L_{corr} = 17 \pm 5$ nm for this series of nominally identical experiments. We note that the dynamics are systematically much cleaner when using liquid alkanes on alkane-only SAMs.

■ INTERPRETATION

In the simple transposition of MKT to mesoscale defects, the activation area was interpreted as the size of a defect. If this is indeed the case, then the task is to find the structure on the surface with the correct size to explain the measured σ. Until now, the defect size was assumed to be the lateral dimension of a gold grain; however, there are other features on the surface that do not scale in the same way as the grains and that may act as pinning sites for a liquid meniscus.

In light of this, one might question whether the SAM can contribute to the disorder, introducing a second length scale to the problem which is relatively constant even when the gold morphology is altered. On atomically flat areas of gold, SAMs are known to produce crystalline domains that can be 5−10 nm in diameter,[18] but it is doubtful that domains can form on a nanoscale roughness. We do not believe that this is an issue here for a number of reasons. First, alkanethiol domain sizes depend on the chain length and termination group, as well as on the conditions of deposition. For example, annealing can produce larger grains or even destroy crystalline order altogether,[18] and it is more difficult to form ordered domains for shorter alkanes where the van der Waals forces between the chains are weaker.[19] We have tried a number of chain lengths (C_6, C_{12}, and C_{18}), as well as termination groups (X = COOCH$_3$ and X = (CF$_2$)$_7$CF$_3$) and temperatures of the deposition solution (50 and 100 °C), and found no significant effect on the activation area. Furthermore, some calculations show that the thiol grain boundary alone should not produce hysteresis,[20] and the same behavior was observed for liquid hydrogen on cesium,[11] where no intermediate layer was used.

Another possible structure are the canyons between grains. Indeed, for the purposes of wetting, they are the most likely defects; the local slope of the surface reflects the wettability, and the areas where it is the greatest are where the contact line is most likely to be pinned. Taking the canyons as defects brings σ closer to the surface characteristics since the canyon size varies less than the grain size in our experiments, but it is not enough. Furthermore, it fails to explain the strong dependence of σ on the liquid.

We propose that the canyons between grains are indeed the pinning centers and that σ depends on the strength of the pinning force, which differs between liquids. This can be quantitatively understood by closer examination of the dynamics of pinning on a single canyon.
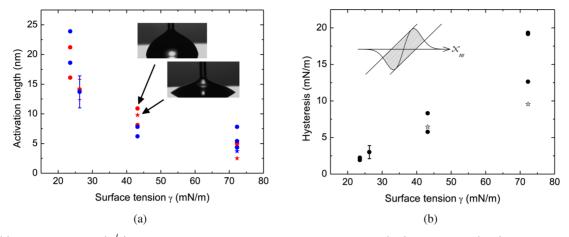
(a)   (b)

Figure 5. (a) Activation lengths ($\sqrt{\sigma}$) deduced from the low velocity dynamics of advancing (red) and receding (blue) contact lines for different liquids on nominally the same surface. Here, the surfaces are 80 nm thick, 25 °C evaporated gold films covered with a dodecanethiol SAM (circles). Also shown (stars) are the activation lengths when changing the thiol end group ($n = 2$, X = COOCH$_3$). Inset photographs illustrate the difference in contact angle for two conditions that yield similar activation lengths. (b) Hysteresis measured in the same experiments. The inset illustrates how the hysteresis can be determined from Figure 6b.

Table 2. Contact Angles (Advancing, Receding; In Degrees) on 25°C Evaporated Gold Films Covered with an Alkanethiol SAM

HS(CH$_2$)$_n$X		liquid			
n	X	decane	tetradecane	DMSO	water
11	CH$_3$	32, 20	39, 26	78, 67	116, 100
2	(CF$_2$)$_7$CF$_3$	65, 46	73, 58	–	–
2	COOCH$_3$	<20	<20	27, –	62, 53

Pinning on a Single Canyon. Insets in Figure 2 show the topography of the canyons between gold grains. Here, we examine how the contact line moves over one such defect of width a perpendicular to the contact line and extent d parallel to the line. Figure 6 illustrates the Joanny−de Gennes model to graphically solve the force balance,[4] which was originally introduced to discuss hysteresis. It has been used to interpret the force curves of single defects measured by AFM[21] and has been found to be in reasonable agreement with the measured hysteresis on nanostructured surfaces with variable defect density.[8] We now use it to examine the jump length for

activated dynamics. This graphical method solves for x_m, the maximum deflection of the contact line due to the defect. A topographical canyon with a height profile $u(x)$ yields a defect force that, in the limit of small slopes and small contact angles,[22] can be written as

$$f_d = \gamma d \sin \theta_{eq} \frac{du}{dx}\big|_{x_m} \tag{3}$$

where $\hat{x}$ is the direction of motion.[23] This is balanced by an elastic restoring force

$$f_e = k(x_\infty - x_m) \tag{4}$$

where x_∞ is the position of the line far from the defect, the spring constant of the line is $k = \pi\gamma \sin^2 \theta_{eq}/\ln(L/d)$, and L is a largescale cutoff length often taken as the distance between defects.[4] The velocity of the contact line is $v = \partial x_\infty/\partial t$. An equivalent picture of a double-well potential is shown in Figure 6c. At zero temperature, the contact line jumps only when the energy barrier has disappeared; this is the spinodal, or depinning threshold, and corresponds to the blue lines in Figure 6 (panels b and c) and a position of the contact line far
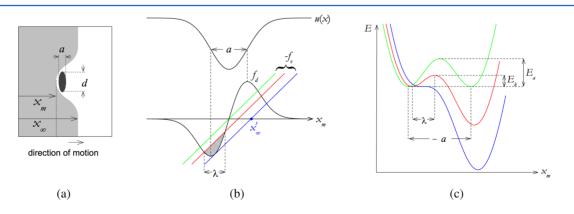

(a)   (b)   (c)

Figure 6. (a) The deformation of the contact line due to a defect of size a in the direction of motion and lateral extent d. (b) Graphical representation of the force balance on a single topographical defect.[4] Above is the profile of the defect of width a and below are the defect force, f_d, and elastic force, f_e, for three different positions of the contact line; x_∞ increases from green to blue. Shown are the configurations when the advancing contact line position has two stable positions (green), when it reaches the spinodal (blue) and when the line jumps the barrier by thermal activation (red). The hatched area corresponds to the energy barrier E_b. (c) The potential well corresponding to the same three positions of the contact line. It is clear that the size of the activated jump λ with respect to the size of the defect a depends on the value of E_a with respect to E_b.

from the defect noted as x_∞^s. At nonzero temperature, thermal activation causes the jump to occur when the energy barrier is small but nonzero (red lines). The activated jump length, λ, corresponds to the distance between the metastable well and the barrier. The rest of the jump, from the barrier to the global minimum, comes for free, energetically speaking. Graphically, it is clear that the activated jump size can be roughly the defect size or significantly smaller. In particular, it is significantly smaller if $E_b \ll E_a$, where E_a is the unbiased energy barrier (found from the Maxwell condition[4] in Figure 6b). Although Figure 6 has been drawn with a symmetric defect force, this need not be the case and, in general, the activation lengths for advancing and receding can differ. It is important to note that we now understand that the activation area is not strictly constant, since λ depends on the magnitude of the energy barrier at which the jump occurs. At very low velocities, there is sufficient time for thermal activation to cause the jump to occur at relatively large barriers and λ will be larger, whereas at higher velocities, the barrier is reduced before the jump can take place and λ will be smaller. At higher velocities still, the dynamics deviate from classical thermal activation since the barriers are small compared to $k_B T$.

From the Single Defect Picture to the Dynamics. In order to model the dynamics, and to relate λ to σ, a macroscopic portion of the contact line must be considered. We take a surface with a number density of defects $n = l^{-2}$ and assume that these defects act independently. In experiments, we impose a constant contact line velocity and, therefore, all positions of the contact line, x_∞, are equally probable. One must remember that experimentally measured velocities and forces are averages over all possible positions of the contact line at the microscopic scale. Consider an elemental length l along the line within which there is on average a single defect. The rate-limiting step for this element of line to move is due to the thermal hopping of the energy barrier provided by the defect. Once this barrier is overcome, the elemental length moves forward by an average distance of l. The macroscopic velocity is thus

$$v = l\langle\tau^{-1}\rangle = l\left[\frac{1}{l}\int_{-l/2}^{l/2}\tau^{-1}\,\mathrm{d}x_\infty\right] \tag{5}$$

where τ^{-1} is an escape rate for the elemental length to make a jump of l.

If the position of the contact line, x_∞, within this elemental length is far from the defect, then the line is in a position with a single minimum and it will not jump ($\tau^{-1} = 0$). As x_∞ approaches the defect, τ^{-1} increases; it is largest near the spinodal, x_∞^s. For small enough velocities, the contact line will have enough time to jump the energy barrier before the spinodal is reached. At a given small velocity, the jump will occur on average at a position defined as x_∞^*. Beyond this point, since the line has already jumped and is in a stable position, it will not jump again ($\tau^{-1} = 0$). We can therefore reduce the limits of integration in eq 5 to only over the defect, giving

$$v = \int_{-a}^{x_\infty^*}\tau^{-1}\,\mathrm{d}x_\infty \tag{6}$$

In writing this, we assume that there is a narrowly distributed range of x_∞ at which a jump occurs, allowing us to impose an abrupt cutoff of the integral at x_∞^*. This can be shown to be the case by explicitly calculating the full probability distribution of x_∞ at which a jump occurs, as is done in the Appendix.

We now need to evaluate τ^{-1} when x_∞ is near the defect and there are two energy minima. In accordance with Kramers' reaction-rate theory,[24] which has recently been used to evaluate the jump frequency in MKT,[25] the Arrhenius escape rate in the case of strong friction ($\alpha \gg \omega_b$) is written

$$\tau^{-1} = \frac{\omega_0\omega_b}{2\pi\alpha}\exp\left(\frac{-E_b}{k_B T}\right) \tag{7}$$

Here α is the viscous friction, and ω_0 and ω_b are the oscillation frequencies at the bottom of the well and at the barrier, respectively. From the single defect picture above, we understand that the shape of the potential well depends strongly on the bias (i.e., the position of the contact line, x_∞). We now search to express this dependence of the energy barrier and of the oscillations frequencies on the bias, choosing to parametrize the problem by the activated jump length, λ. Specifically, we will examine an advancing contact line moving over a single defect centered at $x_m = 0$ and where the activated jump length at which the contact line is most likely to jump satisfies $\lambda^* \ll a$. This last simplifying assumption implies that only the shape of defect force near the peak is important; we approximate it to be parabolic and write it as

$$f_d = A\left(\frac{a}{2} + x_m\right)^2 - f_d^{max} \tag{8}$$

where $A = (1/2)(\mathrm{d}^2 f_d/\mathrm{d}x_m^2)|_{x_s}$ is the curvature. In the parabolic model, the curvature is the same regardless of where it is evaluated. Here, we use the subscript x_s loosely to indicate that A must be evaluated where the model applies (i.e., near the spinodal). From the solutions to the force balance of eqs 4 and 8, it can be shown that the activated jump is

$$\lambda = 2\sqrt{\frac{k}{A}(x_\infty^s - x_\infty)} \tag{9}$$

the shape of the potential well, $E(x_m)$, can be found, and the energy barrier can be written as

$$E_b = \frac{A}{6}\lambda^3 \tag{10}$$

The oscillation frequencies are defined as $\omega_0^2 = (1/M)(\mathrm{d}^2 E/\mathrm{d}x_m^2)|_{well}$ and $\omega_b^2 = (1/M)(\mathrm{d}^2 E/\mathrm{d}x_m^2)|_{barrier}|$, where M is taken to be the mass of the fluid involved in the jump. An expansion around the well minimum and the barrier of the potential studied here yields

$$\omega_0^2 = \omega_b^2 = \frac{A\lambda}{M} \tag{11}$$

Returning to eq 6, we can now make a change of the variable of integration to λ and write

$$v = \frac{-A^2}{4\pi M\alpha k}\int_a^{\lambda^*}\lambda^2\exp\left(\frac{-A\lambda^3}{6k_B T}\right)\mathrm{d}\lambda = v_0\exp\left(\frac{-E_b^*}{k_B T}\right) \tag{12}$$

where $v_0 = Ak_B T/(2\pi\alpha kM)$ and where we have used the notation λ^* and E_b^* to refer to those quantities evaluated when the contact line is at the position where it is most probable to jump, x_∞^*. In the limit examined here ($\lambda^* \ll a$), the escape rate at the bottom limit of integration is negligible and the integral is dominated by the value at λ^*.

We have arrived at eq 12 from the empirical argument used to write eq 6. Although this argument provides some physical

insight into the elementary motion of the contact line, one may wish for a more complete derivation. In fact, eq 12 can be found from the escape-field distribution (the probability distribution of a jump to take place at a position x_∞) for escape from a metastable well subject to a steadily increasing bias. This general problem[26] has been studied in the context of thermal phase slip in Josephson junctions[27] and more recently for the elastic contributions to atomic friction.[13,14,28] In the Appendix, we outline a solution to this problem in contact line variables. As above, we consider the case where the defect force is parabolic near the peak and continue to parametrize the problem with λ. It turns out that this parametrization greatly simplifies the calculation over the previously published[26] solution.

We now search to express the energy barrier, E_b^*, in terms of measurable quantities. Conservation of energy links the macroscopic contact angles and the energy dissipated during a jump of the line from one energy minimum to another.[4] We denote this dissipated energy as W_s when the line jumps at the spinodal and W_d^* when it jumps at x_∞^*,

$$nW_s = \gamma(\cos\theta_{eq} - \cos\theta_A)$$
$$nW_d^* = \gamma(\cos\theta_{eq} - \cos\theta) \qquad (13)$$

where θ_A is now strictly defined as the advancing contact angle at the spinodal. Graphically, the difference in dissipated energy between these two cases corresponds to the shaded areas in Figure 7. In the limit of $\lambda^* \ll \tilde{a}$ it is approximately

$$W_s - W_d^* \approx \tilde{a}\Delta f = \tilde{a}k(x_\infty^s - x_\infty^*) = \frac{A\tilde{a}}{4}(\lambda^*)^2 \qquad (14)$$
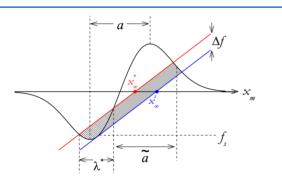

Figure 7. Graphical illustration of the difference in dissipated energy $(W_s - W_d^*)$. In the limit we examine here, $\lambda^* \ll \tilde{a}$, the hatched area is neglected as it is much smaller than the shaded area.

where we have used the previous result from eq 9. If we assume a soft elastic force then we can further write $\tilde{a} \approx f_s/k$. For now, we retain $\tilde{a}$, but keep in mind that as long as we are far from the onset of hysteresis, it can be expressed in terms of experimentally measurable quantities. Using eqs 10, 13, and 14, the energy barrier can now be related to the macroscopic contact angles as

$$E_b^* = \frac{4}{3}\left(\frac{\gamma}{n\tilde{a}}\right)^{3/2}\left(\frac{1}{A}\right)^{1/2}(\cos\theta - \cos\theta_A)^{3/2} \qquad (15)$$

This completes eq 12 to yield the thermally activated dynamics in terms of experimentally measurable quantities. Recapitulating and generalizing for either advancing (A) or receding (R) contact lines, we now write the dynamics as

$$v = v_0 \exp[-\beta(\pm\cos\theta \mp \cos\theta_{A/R})^{3/2}] \qquad (16a)$$

where

$$\beta = \frac{4\sqrt{2}}{3k_BT}\left(\frac{\gamma}{n\tilde{a}}\right)^{3/2}\left(\frac{d^2f_d}{dx^2}\Big|_{x_s}\right)^{-1/2} \qquad (16b)$$

and

$$v_0 = \frac{k_BT}{4\pi\alpha Mk}\frac{d^2f_d}{dx^2}\Big|_{x_s} \qquad (16c)$$

This no longer resembles a simple Arrhenius law. The nonlinear dependence of the force in eq 16a implies that the activation area, or jump length, depends on the velocity. Indeed, the language of jump length no longer appears explicitly; instead, the dynamics are entirely expressed in terms of the surface and liquid properties. The notion of a variation of the jump length with the velocity translates to a curvature in the usual plot of the dynamics, as seen in Figure 3. The velocity prefactor, v_0, is understood to be the limiting velocity for which the contact line dynamics are thermally activated as it corresponds to an $E_b^* = 0$. In many experiments, a limited range of velocities and of contact angles are attained. In this case, eq 16a can be linearized around some working point θ_m to yield

$$v = v_0 \exp\left(-\frac{E_b^m - \sigma\gamma(\pm\cos\theta_m \mp \cos\theta)}{k_BT}\right) \qquad (17)$$

This has the same form as MKT. If one erroneously identifies θ_m as the equilibrium contact angle θ_{eq}, then E_b^m would appear to be the activation free energy of wetting. However, in this linearized equation, its physical interpretation is not simple; it is an offset that varies with the working point, $E_b^m = (A/6)(\lambda_m^*)^3$. On the other hand, the activation area σ can now be expressed as

$$\sigma = \left(\frac{\lambda_m^*}{\tilde{a}}\right)\left(\frac{1}{n}\right) \qquad (18)$$

For the case considered here, $\lambda_m^* \ll \tilde{a}$, we see that the activation area can be considerably smaller than $1/n$, the value obtained in MKT.

We note that averaging over all positions of the contact line blurs the distinction between a and d. Furthermore, in usual conditions, $\tilde{a}$ is of order a, so we will take $\tilde{a} \approx a \approx d$ in what follows.

We can also estimate v_0 in eq 16c. In the case of a moving contact line, viscous forces can be written as

$$f_\eta = M\alpha v \qquad (19)$$

which we assume is valid down to mesoscopic scales. One can write $M\alpha = 3a\eta \ln(L/a)/\theta_{eq}$ for small angles,[29] where $M \approx \rho a^2$ is the mass per unit length of the contact line involved in the jump. It can then be shown that the limiting velocity is of order $v_0 \approx [k_BT/(12\pi^2\eta a^2)](du/dx)|_{max}$, which is in the range of 100 − 1000 μm/s for typical liquids ($\eta \approx 1$ mPa s) on mesoscopically rough surfaces. We expect this to be very similar for all surfaces used since, for example, the high temperature films have larger slopes, but also larger defect sizes, which compensate in the calculation of v_0.

Different Defect Sizes. First, we examine the high-temperature evaporated films and why the activation area

found when fitting to eq 17 is smaller than any features on the surface. An example of a canyon between two large grains on the 200 °C evaporated films is shown in the inset of Figure 2; these larger features do not suffer tip effects to the same extent and one can have some confidence in the slope (45°) and defect width and density (we take $a \approx n^{-1/2} \approx 70$ nm). From eq 18 and the measured activation length of 23 nm on this particular surface, we find $\lambda^* \approx 8$ nm. This clearly falls into the case considered above of $\lambda^* \ll a$ and of jumps that take place close to the spinodal.

In order to understand this, we must compare the unbiased energy barrier E_a and the barrier at which the jump occurs E_b^*. Since the range of velocities and the limiting velocity, v_0, are approximately the same for all surfaces and measurements made here, the range of E_b are the same also. As shown in Figure 3, the slope from which σ is determined is centered about a velocity of 1 μm/s, leading to an E_b^* of roughly $5k_BT$, when using the v_0 estimated above. The precise value of the velocities are of secondary importance since they affect the energy barrier only logarithmically. To obtain E_a, we can approximate the defect force as symmetric and defined piecewise by two parabolas, in which case eq 10 holds at all times. Noting that E_a is the energy barrier when the contact line has two stable solutions (green line in Figure 6) and $\lambda \approx a$, one finds $E_a > 10^3 k_BT$. This is consistent with our understanding that the activated jump can be significantly smaller than the defect size when the activation energy is significantly larger than the energy barrier at which the jump occurs. It is important to note that if one were able to make measurements of the dynamics at much smaller velocities (i.e., a much larger E_b^*) then one would find much larger activation areas, eventually reaching the size of the defect.

In this picture, it is indeed possible to find the same σ for defects that are different in size and in the magnitude of the pinning force, as appears to be the case between the room-temperature and 200 °C films. Again taking the defect force as a piecewise parabola and eqs 10 and 18, one can show that $\sigma^3 = [12E_b^*/(a^3n^3)](d^2f_d/dx^2)^{-1} \approx [12E_b^*/(a^2n^3\gamma \sin \theta_{eq})][(du/dx)|_{max}]^{-1}$, where the final expression uses eq 3. In practice, the energy barrier at which the jumps take place are similar for all substrates and therefore if the maximum slope of the larger grains is at least 10 times larger than for the small grains and the area and distance between defects are 2−3 times larger (not unreasonable values for our surfaces), then the activation areas are similar.

The above arguments only provide order of magnitude estimates; one must be careful when attempting to do a quantitative analysis because the defect size and density and the curvature of the defect force near the peak must be accurately known. Even parameters as simple as the defect size are difficult to determine for such heterogeneous surfaces as in Figure 2. Exacerbating the problem, AFM tip effects can be very important with the room-temperature evaporated films in particular. For example, the profile of a canyon measured by AFM underestimates the real slope, and a very small slope can yield a defect with no hysteresis, which is not the case in experiments. In order to find a hysteresis for small grains using the simple parabolic model, a slope of about 20° is needed, which is larger than that shown in the profile of Figure 2. This illustrates the need for more detailed topographic information to model contact line pinning on such surfaces.

Different Thiols/Liquids. The dependence of the dynamics on the liquid properties can also be deduced from this model. The liquid−vapor surface tension and the contact angle affect both the defect and elastic forces and therefore E_a and σ. When changing the liquid, one changes γ and the contact angle simultaneously and it is difficult to extract how each parameter affects the dynamics. One expects that for larger γ the energy cost in making a jump of a given size increases. Also, one might expect a geometrical effect where for larger contact angles the contact line is more easily pinned.

From Figure 5a, it appears that the activation length is piloted principally by the surface tension. For example, DMSO on a methyl-3-mercaptopropionate SAM has an advancing angle of about 30°, very nearly the same as decane on a dodecanethiol SAM. However, the activation length is about half the size than for the latter and is in fact close to that of DMSO on a dodecanethiol SAM, which has a contact angle of 78°. It is surprising that the contact angle appears to have little effect. It may be that the effect is small here because the maximum slope in the canyons on room-temperature films is small.

If one neglects the effects of the contact angle, both the disorder and elastic forces are simply proportional to γ. Therefore, for the same jump size, the energy barrier scales with γ. Again supposing that the barrier at the most probable jump position, E_b^*, is approximately constant for all substrates, we expect that σ decreases with increasing γ, which is indeed what we find experimentally. The precise form of this dependence depends on the details of the entire shape of the defect force, which we do not know, due to both a lack of detail in the AFM images and a need to modify eq 3 for large contact angles and for large slopes.

Figure 5b shows the measured hysteresis for the same set of substrates as in 5a. In the Joanny−de Gennes model, the hysteresis can be understood graphically from the force balance;[4] the shaded area in the inset corresponds to H divided by the defect density. For substrates that are nominally the same, the defect shape and density are constant and therefore we have only the liquid dependence. We expect that $H \propto \gamma$ and, as noted above for σ, that the dependence on θ is more difficult to understand.

Thermal Activation and Region of Validity. Until now, we have not used the full form of the dynamics as developed in eq 16a but have analyzed experimental data using the linearized form because it allows a discussion in terms of the activation area, which is typically the parameter plotted for these types of measurements. We now return to the full form and recall the conditions under which this model is valid: (1) the defects have been assumed to be independent, (2) we have assumed the case of strong friction in order to evaluate the Kramers prefactor, (3) $\lambda^* \ll a$ in order to satisfy the parabolic approximation of the defect force, and (4) more generally, we require that $E_b^* \gg k_BT$, in order for Kramers' rate to be valid.

The first assumption amounts to neglecting collective effects. This is a severe approximation given the defect density on gold films; however, we note that the experimental jump sizes are at most the size of a single gold grain, so this may not be as unreasonable as it first appears. The second can be checked for our surfaces from arguments following eq 19. We take the logarithmic factor to be on the order of unity and find $\alpha \approx 10^9$ Hz for the liquids and surfaces used here. The frequency at the well minimum scales as $\omega_0 \approx [f_d^{max}/(Ma^2)]^{1/2} \approx 10^8$ Hz and strong friction applies. The Kramers prefactor is therefore approximately 10^6 Hz, in reasonable agreement with estimates obtained from scaling arguments.[30] Since we are no longer

talking about molecular displacements, it is expected that this is smaller than the thermal frequency of nearly 10^{13} Hz often used in MKT.

From Figure 6c, one can see that the third condition implies that $E_a \gg E_b^*$. The unbiased energy barrier is not easily calculated, since the full form of the defect force must be known; however, some dependencies can be deduced from the graphical picture in Figure 6b. For example, $E_a \propto \gamma$ since both the defect and the elastic forces are proportional to the surface tension. Also, E_a increases with increasing du/dx since the defect force is proportional to the local slope. Thus, eq 16a best represents the dynamics on highly sloped surfaces partially wetted by high surface tension liquids.

The last condition can be understood as limiting the velocity for which thermally activated motion is obtained. Since $E_b^*/(k_BT) = \ln(v_0/v) \gg 1$, experimental velocities must be significantly smaller than v_0, which we can now estimate from measurable surface and liquid properties using eq 16c. This limit scales with viscosity; an indicative value for each liquid used here is given in Table 1. This velocity is within the range of experimental conditions and is indeed very close to where the dynamics clearly change character in Figure 3. The condition $v = v_0$ corresponds to the spinodal and beyond this notions of thermal activation break down. Strictly speaking, since $\ln(v_0/v) \approx 1$ in experiments, eq 16a cannot be used to model experimental data this close to the spinodal. Although not rigorously within the region of validity, we have performed an experiment for which the condition on $\ln(v_0/v)$ is the most reasonable (e.g., decane, the liquid with the smallest viscosity), and we have used a piezo-driven stage to obtain extremely low velocities, down to 1 nm/s. Figure 8 shows the advancing dynamics fit to eq 16a, where only velocities ≤ 20 μm/s are used. We have fixed the spinodal velocity v_0 according to Table 1 and left only 2 adjustable parameters: θ_A and β. The resulting fit is good and accounts for the curvature of the model up to the spinodal. It can be shown that β scales as $[\gamma a^2 \sin \theta_{eq}/(k_BT)][(du/dx)|_{max}]^{-2} \approx 10^3$, in agreement with the magnitude
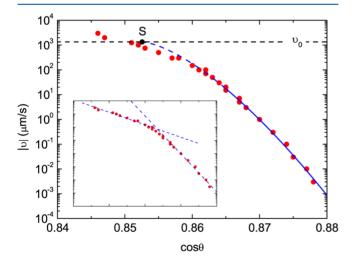

Figure 8. Wetting dynamics of liquid decane advancing on a gold surface evaporated at 25 °C and coated with a SAM of dodecanethiol. In the main figure, low velocity data has been fit to eq 16a (solid blue line), as described in the text. The dashed portion of the blue line shows the fit extrapolated up to the spinodal (S). The inset shows two fits to eq 2: over the same low velocity range and at high velocity. The latter illustrates how the use of thermal activation in an erroneous domain can lead to an underestimation of the activation area σ.

of the fit in Figure 8. Owing to the use of the model outside of its strict range of validity, one must be careful not to over interpret the fit parameters. It is possible to extend Kramers such that it holds near to the spinodal,[31,32] but knowledge of the shape of the potential well is required.

From the model of eq 16, we have been able to show that (1) the curvature in the thermally activated dynamics is a natural consequence of a constantly increasing bias and (2) the region of validity of thermal activation is limited to very low velocities, typically less than 1 mm/s for usual liquids on mesoscopically rough surfaces. The latter is an important observation because over a restricted range of velocities, mathematically one can usually fit experimental dynamics to a thermally activated law. For example, the inset in Figure 8 shows two fits to the exponential law of eq 2, one at the usual low velocities considered here (≤ 20 μm/s) and the other at higher velocities. The latter misleadingly yields a considerably smaller σ. This may explain why in some experiments using alkanethiol on gold[33] or evaporated titania surfaces,[10] activation lengths of the order of 1 nm or less have been obtained.

Models of thermal activation implicitly assume that the time spent by the contact line to relax is negligible compared to the waiting time in the potential well. However, under certain conditions, viscous effects can pilot the time for the contact line to relax and reach the stable position when it jumps from the spinodal. This so-called disanchoring dynamics of a single defect under fixed velocity has been studied,[34] and the contact line was found to maintain its shape near the spinodal for a time t_α before relaxing exponentially.[35] The corresponding velocity is of the order of $a/t_\alpha = [vk^2/(\alpha^2M^2)]^{1/3} \approx 10$ cm/s for $v = 20$ μm/s. Since this is much faster than the contact line velocities used here, the neglect of viscous dissipation in the activated dynamics is justified.

One can also ask what controls the dynamics beyond v_0. Hydrodynamic models such as Cox−Voïnov[5] are often used to describe the contact line dynamics at higher velocity. However, for reasonable choices of the micro- and macroscopic cutoff scales that appear in this model, one finds a weaker dependence of the contact angle on the velocity than is shown at the highest velocities in Figure 8. This suggests that at the highest velocities tested here, the contact line remains close to the depinning threshold and a truly viscous regime has not yet been attained. In addition, collective effects may play a role in this intermediate region. In this case, one expects to find a signature of the critical dynamics generic to disordered elastic systems[1] and which is characterized by a depinning exponent[5] that is subject to theoretical debate. How the low-velocity dynamics are connected to the viscous regime is an interesting outstanding question, one which we now understand requires velocities spanning from the very low values obtained here to considerably higher velocities, all in the same experimental setup.

■ CONCLUSION

We have studied thermally activated dynamics of a contact line over a range of controlled nanotopographies and a range of partially wetting liquids. The activation area is found to change very little despite apparently large changes in the topography and can be significantly smaller than the lateral scale of the disorder. The liquid surface tension has a strong effect on the activation area. These observations can be understood with the simple model of contact line pinning where the defects correspond to topographical canyons and the contact line is

very near the depinning threshold. These more complicated dynamics can be explicitly written entirely in terms of the surface and liquid properties, which has been done here for the simple limit of independent defects. In this model, the activation area is seen to depend on the pinning strength of the defect, the velocity of the contact line, and the density of defects. The influence of the first two are illustrated in experiments presented here. In order to investigate the dependence on the shape and density of defects, more controlled surfaces are required: a problem that we are currently pursuing.

■ APPENDIX

Here, we examine the escape-field distribution for escape from a metastable well subject to a steadily increasing bias. The probability that a jump has not yet taken place by a time t is

$$W\{\lambda[x_\infty(t)]\} = \exp\left[-\int_{-\infty}^{t} \frac{1}{\tau(t')}\, dt'\right] \tag{20}$$

from which we can find the distribution of jump positions

$$P[x_\infty] = -\frac{dW}{dx_\infty} \tag{21}$$

A simple change of variables of integration ($t' \to \lambda'$) using eq 9 and introducing the (constant) velocity of the contact line as $x_\infty = vt$ yields

$$W[\lambda] = \exp\left[\frac{-v_0}{v} \exp\left(\frac{-\lambda}{\lambda_0}\right)^3\right] \tag{22}$$

which in turn yields

$$P[x_\infty] = \frac{A\lambda}{2\pi\alpha M v} \exp\left(\frac{-\lambda}{\lambda_0}\right)^3 \exp\left[\frac{-v_0}{v} \exp\left(\frac{-\lambda}{\lambda_0}\right)^3\right] \tag{23}$$

For convenience, we have introduced the notation $(\lambda/\lambda_0)^3 = E_b/(k_B T)$. One must be careful with the notation used here: x_∞ is uniformly distributed in the case of constant contact line velocity, and $P[x_\infty]$ represents the distribution of x_∞ at which a jump occurs. From the full probability distribution, the position of the contact line at which a jump is most probable (x_∞^*) can be found:

$$0 = \frac{dP}{dx_\infty}\Big|_{x_\infty^*}$$

$$= \frac{-k}{\pi\alpha M v \lambda^*} \exp\left(\frac{-\lambda^*}{\lambda_0}\right)^3 \exp\left[\frac{-v_0}{v} \exp\left(\frac{-\lambda^*}{\lambda_0}\right)^3\right] g(\lambda^*) \tag{24}$$

where

$$g(\lambda^*) = 1 - 3\left(\frac{\lambda^*}{\lambda_0}\right)^3 + 3\frac{v_0}{v}\left(\frac{\lambda^*}{\lambda_0}\right)^3 \exp\left(\frac{-\lambda^*}{\lambda_0}\right)^3$$

$$\approx -3\left(\frac{\lambda^*}{\lambda_0}\right)^3\left[1 - \frac{v_0}{v} \exp\left(\frac{-\lambda^*}{\lambda_0}\right)^3\right] \tag{25}$$

For Kramers' rate and the usual notions of thermal activation to hold, $(\lambda/\lambda_0)^3 = E_b/(k_B T) \gg 1$, so the first term in eq 25 can be neglected to obtain the right-most expression. The maximum probability occurs for $g(\lambda^*) = 0$, yielding exactly eq 12.

■ AUTHOR INFORMATION

Corresponding Author

*E-mail: kristina.davitt@lps.ens.fr.

Notes

The authors declare no competing financial interest.

■ REFERENCES

(1) Agoritsas, E.; Lecomte, V.; Giamarchi, T. Disordered elastic systems and one-dimensional interfaces. *Phys. B* **2012**, *407*, 1725−1733.

(2) Metaxas, P.; Jamet, J.; Mougin, A.; Cormier, M.; Ferré, J.; Baltz, V.; Rodmacq, B.; Dieny, B.; Stamps, R. Creep and flow regimes of magnetic domain-wall motion in ultrathin Pt/Co/Pt films with perpendicular anisotropy. *Phys. Rev. Lett.* **2007**, *99*, 217208.

(3) Laurson, L.; Santucci, S.; Zapperi, S. Avalanches and clusters in planar crack front propagation. *Phys. Rev. E: Stat., Nonlinear, Soft Matter Phys.* **2010**, *81*, 046116.

(4) Joanny, J. F.; de Gennes, P. G. A model for contact angle hysteresis. *J. Chem. Phys.* **1984**, *81*, 552−562.

(5) Bonn, D.; Eggers, J.; Indekeu, J.; Meunier, J.; Rolley, E. Wetting and spreading. *Rev. Mod. Phys.* **2009**, *81*, 739−805 and references therein.

(6) Blake, T.; Haynes, J. Kinetics of liquid/liquid displacement. *J. Colloid Interface Sci.* **1969**, *30*, 421−423.

(7) Abe, K.; Takiguchi, H.; Tamada, K. Dynamic contact angle measurement of Au(111)−Thiol self-assembled monolayers by the Wilhelmy plate method. *Langmuir* **2000**, *16*, 2394−2397.

(8) Ramos, S. M. M.; Charlaix, E.; Benyagoub, A.; Toulemonde, M. Wetting on nanorough surfaces. *Phys. Rev. E: Stat., Nonlinear, Soft Matter Phys.* **2003**, *67*, 031604.

(9) Semal, S.; Blake, T. D.; Geskin, V.; de Ruijter, M. J.; Castelein, G.; De Coninck, J. Influence of surface roughness on wetting dynamics. *Langmuir* **1999**, *15*, 8765−8770.

(10) Fetzer, R.; Ralston, J. Dynamic dewetting regimes explored. *J. Phys. Chem. C* **2009**, *113*, 8888−8894.

(11) Rolley, E.; Guthmann, C. Dynamics and hysteresis of the contact line between liquid hydrogen and cesium substrates. *Phys. Rev. Lett.* **2007**, *98*, 166105.

(12) We note that for a contact line close to θ_{eq}, thermal activation can occur in both the advancing and receding directions and that MKT is sometimes written as a sum of eq 2 for both directions in order to reflect this,[6] leading to a hyperbolic sine function. Although θ_{eq} is not experimentally measurable (because of hysteresis), from the fact that the hysteresis is large, we can infer that we are far from equilibrium in all experimental conditions examined here. In this case, the energy barrier to motion in the direction of the macroscopic line velocity (say, advancing) is very small, whereas in the other (receding) it is very large, which is why a single exponential suffices here.

(13) Sang, Y.; Dubé, M.; Grant, M. Thermal effects on atomic. *Phys. Rev. Lett.* **2001**, *87*, 174301.

(14) Caroli, C.; Nozières, P. In *Physics of Sliding Friction*; Persson, B.; Tosatti, E., Eds.; Kluwer Academic Publishers: Norwell, MA, 1996; pp 27−49.

(15) Semaltianos, N.; Wilson, E. Investigation of the surface morphology of thermally evaporated thin gold films on mica, glass, silicon and calcium fluoride substrates by scanning tunneling microscopy. *Thin Solid Films* **2000**, *366*, 111−116.

(16) Higo, M.; Fujita, K.; Tanaka, Y.; Mitsushio, M.; Yoshidome, T. Surface morphology of metal films deposited on mica at various temperatures observed by atomic force microscopy. *Appl. Surf. Sci.* **2006**, *252*, 5083−5099.

(17) Fubel, A.; Zech, M.; Leiderer, P.; Klier, J.; Shikin, V. Analysis of roughness of Cs surfaces via evaluation of the autocorrelation function. *Surf. Sci.* **2007**, *601*, 1684−1692.

(18) Delamarche, E.; Michel, B.; Kang, H.; Gerber, C. Thermal stability of self-assembled monolayers. *Langmuir* **1994**, *10*, 4103−4108.

(19) Laibinis, P.; Whitesides, G.; Allara, D.; Tao, Y.-T.; Parikh, A.; Nuzzo, R. Comparison of the structures and wetting properties of self-assembled monolayers of *n*-alkanethiols on the coinage metal surfaces, Cu, Ag, Au. *J. Am. Chem. Soc.* **1991**, *113*, 7152−7167.

(20) Sams, A. N.; Merten, V. E.; Pettersen, M. S. APS physics. Experimental and numerical study of the role of disorder on contact angle hysteresis. http://meetings.aps.org/Meeting/MAR12/Event/162271; accessed May 13, 2013.

(21) Delmas, M.; Monthioux, M.; Ondarçuhu, T. Contact Angle Hysteresis at the Nanometer Scale. *Phys. Rev. Lett.* **2011**, *106*, 136102.

(22) de Gennes, P. G. Wetting: statics and dynamics. *Rev. Mod. Phys.* **1985**, *57*, 827−863.

(23) We have introduced the extent d. In its original form,[4] the defect force is written as $f_d \simeq \int_{-\infty}^{+\infty} h(x_m, y) \, dy$ where for topographical defects[22] $h(x,y) = \gamma \sin \theta_{eq} [\partial u(x,y)/\partial x]$.

(24) Hänggi, P.; Talkner, P.; Borkovec, M. Reaction-rate theory: Fifty years after Kramers. *Rev. Mod. Phys.* **1990**, *62*, 251−341.

(25) Blake, T.; Coninck, J. D. Dynamics of wetting and Kramers' theory. *Eur. Phys. J.: Spec. Top.* **2011**, *197*, 249−264.

(26) Garg, A. Escape-field distribution for escape from a metastable potential well subject to a steadily increasing bias field. *Phys. Rev. B: Condens. Matter Mater. Phys.* **1995**, *51*, 15592−15595.

(27) Kurkijärvi, J. Intrinsic fluctuations in a superconducting ring closed with a Josephson junction. *Phys. Rev. B: Condens. Matter Mater. Phys.* **1972**, *6*, 832−835.

(28) Sang, Y.; Dubé, M.; Grant, M. Dependence of friction on roughness, velocity, and temperature. *Phys. Rev. E: Stat., Nonlinear, Soft Matter Phys.* **2008**, *77*, 036123.

(29) de Gennes, P. G. Surface and interphase physics: Dynamics of a triple line. *C. R. Acad. Sci. Paris* **1986**, *302*, 731−733.

(30) Snoeijer, J. H.; Andreotti, B. Moving contact lines: Scales, regimes and dynamical transitions. *Annu. Rev. Fluid Mech.* **2013**, *45*, 269−292.

(31) Cristiano, R.; Silvestrini, P. Aspects of thermal activation theory and applications to the Josephson effect. *J. Appl. Phys.* **1986**, *60*, 3243−3246.

(32) Ambegaokar, V.; Halperin, B. Voltage due to thermal noise in DC Josephson effect. *Phys. Rev. Lett.* **1969**, *22*, 1364−1366.

(33) Voué, M.; Rioboo, R.; Adao, M. H.; Conti, J.; Bondar, A. I.; Ivanov, D. A.; Blake, T. D.; De Coninck, J. Contact-line friction of liquid drops on self-assembled monolayers: Chainlength effects. *Langmuir* **2007**, *23*, 4695−4699.

(34) Raphaël, E.; DeGennes, P. G. Dynamics of wetting with nonideal surfaces. The single defect problem. *J. Chem. Phys.* **1989**, *90*, 7577−7584.

(35) Our notation t_α corresponds to α in the original work,[34] and we have used $\mu_m = 1/(a\alpha M)$, consistent with the definition in eq 19.